

# Bolaform Surfactant-Induced Au Nanoparticle Assemblies for Reliable Solution-Based Surface-Enhanced Raman Scattering Detection

Daniel García-Lojo, David Méndez-Merino, Ignacio Pérez-Juste, Ángel Acuña, Luís García-Río, Alfonso Rodríguez-Patón, Isabel Pastoriza-Santos,\* and Jorge Pérez-Juste\*

Solution-based surface-enhanced Raman scattering (SERS) detection typically involves the aggregation of citrate-stabilized Au nanoparticles into colloidal assemblies. Although this sensing methodology offers excellent prospects for sensitivity, portability, and speed, it is still challenging to control the assembly process by a salting-out effect, which affects the reproducibility of the assemblies and, therefore, the reliability of the analysis. This work presents an alternative approach that uses a bolaform surfactant, B<sub>20</sub>, to induce the plasmonic assembly. The decrease of the surface charge and the bridging effect, both promoted by the adsorption of B<sub>20</sub>, are hypothesized as the key points governing the assembly. Furthermore, molecular dynamic simulations supported the bridging effect of the B<sub>20</sub> by showing the preferential bridging of surfactant monomers between two adjacent Au(111) slabs. The colloidal assemblies showed excellent SERS capabilities towards the rapid, on-site detection and quantification of beta-blockers and analgesic drugs in the nanomolar regime, with a portable Raman device. Interestingly, the application of state-of-the-art convolutional neural networks, such as ResNet, allows a 100% accuracy in classifying the concentration of different binary mixtures. Finally, the colloidal approach was successfully implemented in a millifluidic chip allowing the automation of the whole process, as well as improving the performance of the sensor in terms of speed, reliability, and reusability without affecting its sensitivity.


science, environmental science, or bio-analytical science.<sup>[1–3]</sup> The SERS enhancement is related to a combination of electromagnetic and chemical effects, being 10<sup>10</sup> a reasonable maximum value for the enhancement factor of the Raman signal.<sup>[4]</sup> Considering that the electromagnetic effect is the dominant one, the ability to achieve high SERS enhancements, and therefore high sensing capabilities, often relies on the plasmonic efficiency of the metal surface. In this regard, although discrete plasmonic nanoparticles can obtain reasonable SERS enhancements, their assembly gives rise to higher enhancement factors due to the amplification of the electromagnetic field confined in the gap between closely coupled nanoparticles (known as hot spots).<sup>[5]</sup> Therefore great effort has been devoted to designing and fabricating different substrates based on the assembly of nanoparticles for direct SERS sensing. Significantly, it is still challenging to synthesize/fabricate substrates with outstanding sensing capabilities in terms of efficiency, uniformity, and reliability.<sup>[1,6,7]</sup>

The simplest approach to induce the assembly/aggregation of the nanoparticles is to produce its destabilization. For instance, the destabilization of charged nanoparticles dispersions, where the interparticle forces are dominated by the van der Waals attraction and the electrostatic double-layer repulsion, occurs by screening the electrostatic

## 1. Introduction

The discovery of the Surface-enhanced Raman scattering (SERS) effect last century paved the way for the development of sensing applications in different fields such as materials

D. García-Lojo, I. Pérez-Juste, I. Pastoriza-Santos, J. Pérez-Juste  
CINBIO  
Universidade de Vigo  
Departamento de Química Física  
Campus Universitario As Lagoas  
Marcosende, Vigo 36310, Spain  
E-mail: pastoriza@uvigo.es; juste@uvigo.es

 The ORCID identification number(s) for the author(s) of this article can be found under <https://doi.org/10.1002/admt.202101726>.

© 2022 The Authors. Advanced Materials Technologies published by Wiley-VCH GmbH. This is an open access article under the terms of the Creative Commons Attribution License, which permits use, distribution and reproduction in any medium, provided the original work is properly cited.

DOI: 10.1002/admt.202101726

D. García-Lojo, I. Pastoriza-Santos, J. Pérez-Juste  
Galicia Sur Health Research Institute (IIS Galicia Sur)  
SERGAS-UVIGO  
Vigo 36310, Spain

D. Méndez-Merino, A. Rodríguez-Patón  
Departamento de Inteligencia Artificial  
Universidad Politécnica de Madrid  
Campus de Montegancedo, Boadilla del Monte, Madrid 28660, Spain  
Á. Acuña, L. García-Río  
Departamento de Química Física  
Facultad de Química  
Universidade de Santiago de Compostela  
Santiago 15782, Spain

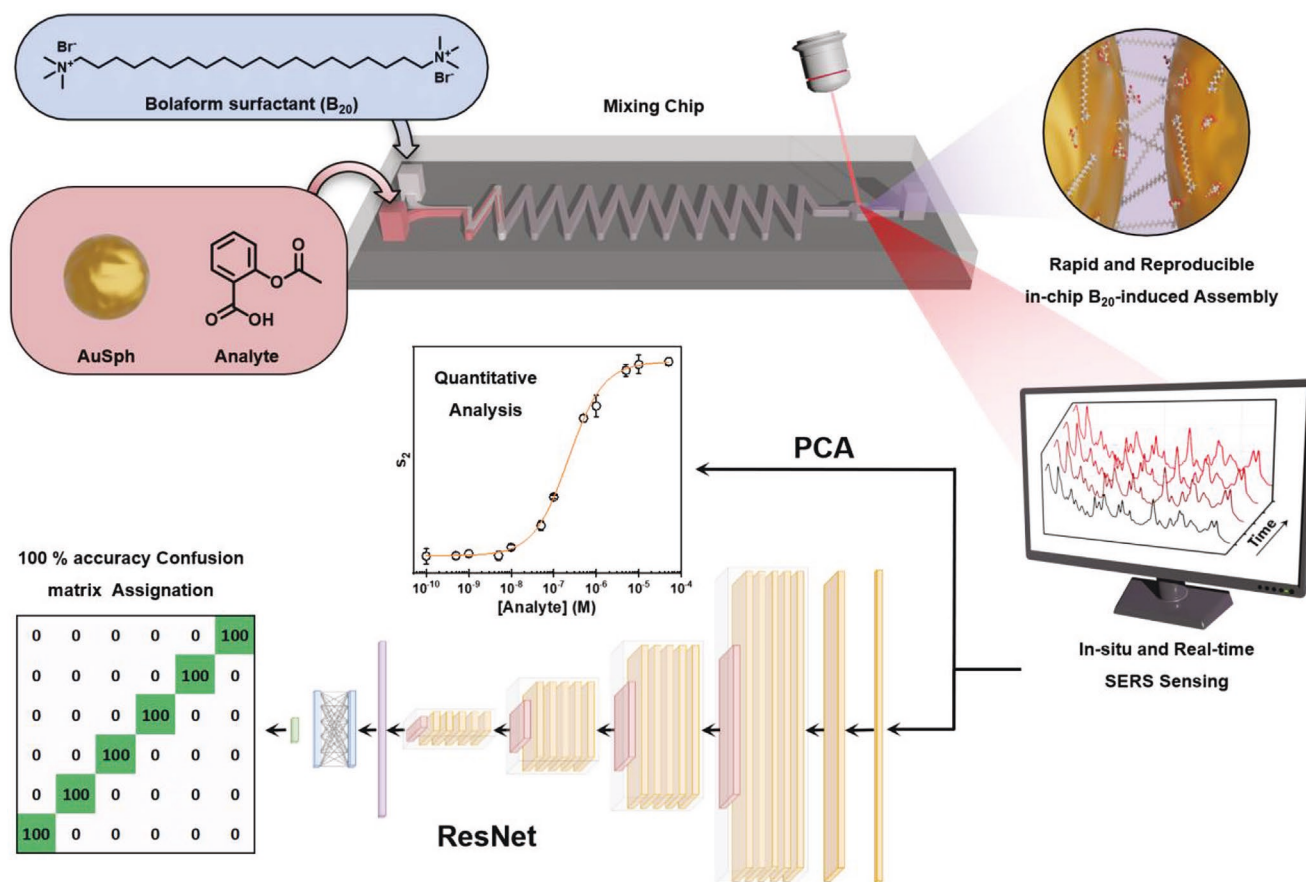


**Figure 1.** Schematic representation of the surface-enhanced Raman scattering (SERS)-based sensing approach. The bolaform surfactant, B<sub>20</sub>, induces the assembly of Au spheres (AuSphs) assembly after mixing inside a millifluidic chip. In the presence of an analyte of interest, it is trapped at the formed hot spots and in-situ detected via SERS analysis with a portable Raman. The SERS data is subsequently treated using principal component analysis (PCA) or deep learning.

double-layer repulsion upon increasing the ionic strength.<sup>[8]</sup> Over the past decades, several experimental studies have demonstrated that the stability-instability of nanoparticles dispersions can be well described with the Derjaguin, Landau, Verwey, and Overbeek (DLVO) theory.<sup>[8,9]</sup> Unfortunately, in the case of citrate-stabilized gold nanoparticles, the irreproducible performance of the aggregation process hinders its practical application as SERS substrate.<sup>[10]</sup> In this context, it is challenging to control the assembly/aggregation of citrate-stabilized nanoparticles in a high reproducibility manner by a salting-out effect.<sup>[11,12]</sup>

The assembly of plasmonic nanoparticles in a fully controlled manner generally requires its surface functionalization with ligand molecules bearing a variety of functional groups.<sup>[13]</sup> These terminal groups have been used to direct the reversible assembly of nanoparticles upon external stimuli, which can be chemical or physical. Unfortunately, this approach hampers the control over the gap between nanoparticles with subnanometric precision, which is a key issue for achieving highly intense and reproducible hot spots.

Alternatively, different molecules with a high affinity toward gold surfaces have been proposed as a trigger to induce aggregation. For instance, Mahajan et al. reported the use of cucurbit[*n*]uril macrocycles (CB[*n*]) to produce the controllable

and highly reproducible aggregation of citrate-stabilized gold nanoparticles.<sup>[14]</sup> The CB[*n*] adsorption to metallic surfaces by electrostatic interactions triggers the formation of dynamic assembly of nanoparticles with a precise gap junction between particles.<sup>[15,16]</sup> These colloidal assemblies have demonstrated good capabilities for SERS sensing, not just because of the reproducible hot spots but also for macrocycle's host-guest capabilities that allow the precise positioning of the analyte on the hot spot.<sup>[17,18]</sup>

Herein, we propose the use of a cationic  $\alpha,\omega$ -type (bolaform) surfactant, eicosane-1,20-bis(trimethylammonium) dibromide (B<sub>20</sub>), to induce the aggregation of citrate-stabilized Au nanoparticles to give rise to reliable plasmonic assemblies. We hypothesized that upon the addition of B<sub>20</sub>, the bolaform surfactant monomers would be readily adsorbed to gold surfaces through quaternary ammonium head groups decreasing the surface charge and promoting an interparticle bridging effect.<sup>[19]</sup> Next, we investigated B<sub>20</sub>-induced AuSph assemblies as a reliable sensing platform for SERS analysis of aqueous-based solutions (Figure 1) employing a handheld Raman spectrometer. Besides, we demonstrated the versatility of this approach for multiplexing experiments in combination with deep learning techniques, such as multilayer neuronal network (MNN) and residual neuronal network (ResNet). Finally, we

integrated the  $B_{20}$ -induced AuSph methodology into a millifluidic system to fabricate a high-performance sensing platform regarding reusability, reproducibility and sensitivity.

## 2. Results and Discussion

### 2.1. Bolaform Surfactant-Induced Assembly

First, we investigated the colloidal assembly of AuSphs triggered by the fast addition of the cationic bolaform surfactant ( $B_{20}$ ). The  $B_{20}$  surfactant is characterized by two terminal quaternary ammonium surfactants that are separated by an aliphatic chain of 20 carbons (Scheme S1A, Supporting Information). AuSph with an average diameter of  $61.3 \pm 5.5$  nm.<sup>[20]</sup> (see Figure S1 in the Supporting Information) were selected as plasmonic building blocks. The citrate ions adsorbed on the metal surface provide AuSph colloidal stability through electrostatic interaction. The  $\zeta$ -potential of AuSph is  $-43.2 \pm 0.9$  mV.

In a typical experiment, a certain amount of  $B_{20}$  was added to a colloidal AuSph dispersion (0.5 mM in terms of  $Au^0$ ), and the assembly process was followed by UV-vis-NIR spectroscopy. Figure 2A–C and Figure S2 in the SI show the time evolution extinction spectra of Au colloids upon addition of different  $B_{20}$  concentrations (ranging the final concentrations from  $10^{-9}$  to  $10^{-1}$  M). Regardless of the amount added, the assembly process reached equilibrium in less than 5 min (Figure S2G in

SI). Therefore, the  $\zeta$ -potential, as well as the hydrodynamic diameter, of the Au colloids were measured 5 min after  $B_{20}$  addition (Figure 2D). Interestingly, the analysis of the data revealed three well-differentiated regimes as a function of the  $B_{20}$  concentration:

i) Low-concentration regime ( $<10^{-7}$  M) where no nanoparticle assembly occurs. Thus, the hydrodynamic diameter of Au colloids (Figure 2D) and, therefore, their optical properties remain unaltered (Figure 2A). A slight increase of the  $\zeta$ -potential from  $-43.2$  mV to  $-30.0$  mV is the only observed effect., most probably due to the adsorption of the  $B_{20}$  monomers.

ii) Assembly regime ( $10^{-7} - 10^{-4}$  M) where a fast AuSph assembly process takes place within less than 5 minutes (Figure 2B,C and Figure S2B-E in the SI), as demonstrated by the decrease in the characteristic localized surface plasmon resonance (LSPR) band of AuSph and the appearance of a new band at higher wavelengths. In addition, dynamic light scattering (DLS) (Figure 2D) and scanning electron microscopy (SEM) (Figure S3, Supporting Information) characterization confirmed the presence of aggregates with average hydrodynamic diameters above 1 micrometre. Interestingly, at this concentration range, the analysis of  $\zeta$ -potential showed values between  $-20.0$  mV to  $+20.0$  mV (Figure 2D), indicating that nanoparticles were below the surface charge stability regime.<sup>[21]</sup> Therefore, the lower surface charge, together with the bridging effect mediated by the  $B_{20}$  (with two quaternary amines heads), could make the AuSph prone to assemble. It should be pointed out that the assembly process is highly reproducible,

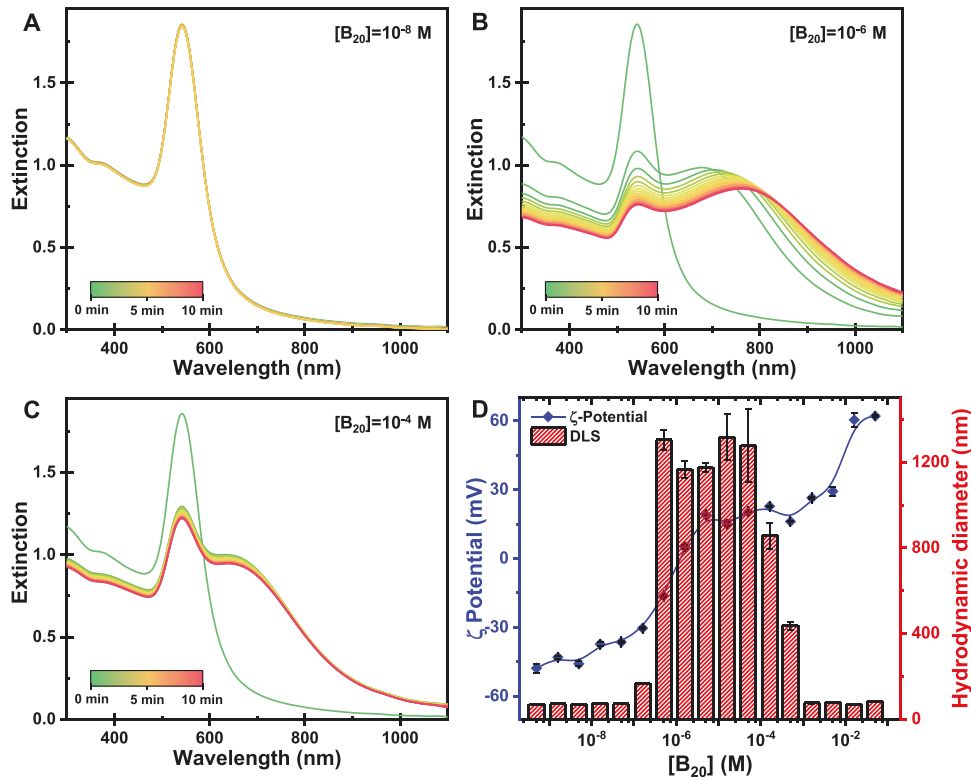


**Figure 2.** Effect of  $B_{20}$  concentration on AuSph assembly. A–C) Time evolution of extinction spectra of colloidal AuSphs upon addition of different concentrations of  $B_{20}$ ;  $10^{-8}$  M (A),  $10^{-6}$  M (B), and  $10^{-4}$  M (C). D)  $\zeta$ -Potential and hydrodynamic diameter of AuSphs as a function of  $B_{20}$  concentration. All measurements were performed 5 min after  $B_{20}$  addition.

as demonstrated by the relatively low variability of the optical properties of AuSph aggregates obtained from 15 independent experiments (see Figure S4 in the SI).

iii) High-concentration regime ( $>10^{-4}$  M) without AuSph assembly. Similar to the “low-concentration regime”, the addition of B<sub>20</sub> did not produce significant changes in the particle size or optical properties (and Figure 2D and Figure S2F in the SI, respectively). In this regime, the surface  $\zeta$ -potential is above +20.0 mV; therefore, the fast addition of B<sub>20</sub> gave rise to the surface charge reversal at the particle surface via molecule adsorption without compromising the colloidal stability.

To summarize, upon adding B<sub>20</sub>, the monomers will adsorb to the nanoparticle surface, decreasing the surface charge slightly but enough to maintain the colloidal stability of the AuSphs. As the B<sub>20</sub> concentration increases, its further adsorption decreases the surface charge to values below the surface charge stability regime. Under these conditions, when two particles are close enough, the B<sub>20</sub> could induce surfactant bridges between them mediated by the favorable interaction of its terminal quaternary ammonium head groups (see Scheme S1A in the SI) and the nanoparticle surface. The combination of the surface charge decreasing within the bridging effect is hypothesized as the key parameters to govern the assembly in a broad range of bolaform surfactant concentrations.

To shine some light on the proposed mechanism, similar experiments were performed with a single-headed quaternary ammonium surfactant with 16 carbons in the aliphatic chain, such as hexadecyltrimethylammonium bromide (CTAB, see Scheme S1B in the SI). As shown in Figure S5 in the SI, at low CTAB concentration (below  $10^{-6}$  M), the optical properties and nanoparticle size didn't change upon CTAB addition, indicating the absence of AuSph aggregation. This behaviour agrees with the  $\zeta$ -potential of the particles, which remain above -30 mV at this concentration range. Nevertheless, the addition of  $1.6 \times 10^{-6}$  M CTAB strongly affected the inherent nanoparticle stability producing a strong aggregation (Figure S5A in the SI) by lowering the AuSph surface charge to values close to zero. Surprisingly, AuSph colloids remained fully stable for CTAB concentrations higher than  $10^{-5}$  M since the complete reversal surface charge ( $>+20.0$  mV) was observed. These results indicated that in the case of CTAB, the AuSph colloids destabilization occurs in a concise concentration range. In contrast, in the case of B<sub>20</sub>, it takes place in a more controlled fashion within a concentration range from  $10^{-7}$  –  $10^{-4}$  M. Moreover, while in the case of CTAB the AuSph aggregation is triggered by the surface charge neutralization, in the case of B<sub>20</sub> the bridging effect may also play a fundamental role.

## 2.2. Molecular Dynamics Simulations

To better understand the interaction between B<sub>20</sub> and AuSph and confirm the hypothesis mentioned above, all atom molecular dynamics (MD) simulations were performed. First, the adsorption of a single B<sub>20</sub> molecule on an Au(111) surface was simulated and compared with the adsorption of a single hexadecyltrimethylammonium cation (CTA) (Figure S6 and see Section 2 in the SI for further details). Simulations showed that both molecules are adsorbed flat on the gold surface,

adopting a stretched configuration where the carbon atoms of the hydrophilic chain accommodate approximately in the space between the lines of gold atoms avoiding direct contact with the atoms on the surface. Interestingly, the adsorption of B<sub>20</sub> ( $E_{\text{ads}}(\text{B}_{20}) = -154.0$  kJ mol<sup>-1</sup>) is energetically more favorable than for CTA ( $E_{\text{ads}}(\text{CTA}) = -134.0$  kJ mol<sup>-1</sup>), probably due to the presence of the second ammonium head group in B<sub>20</sub>.

To evaluate the possibility of B<sub>20</sub> to establish a bridging effect between AuSph, we built up a group of models composed of two Au(111) slabs separated at different distances (from 15 to 35 Å) containing a single B<sub>20</sub> molecule. The snapshots and analysis of number densities show that for distances between 20 and 30 Å, B<sub>20</sub> can adopt configurations contacting simultaneously with the separated Au slabs (Figure 3A and Figure S8 in the SI). The contacts take place through the ammonium groups at the edges of the molecule. For separations between 20 and 25 Å, even a section of the hydrophobic tail seems to contribute slightly to the interaction. No bridging was observed at short separations (<15 Å) because it requires a significant deformation of the alkyl chain, while at large ones (>35 Å), no bridging could be observed because the molecule length is much smaller than the distance between both metallic surfaces (the N-N distance in a stretched ideal hydrocarbon chain of B<sub>20</sub> is approximately 27 Å) (see Figure S8 in the SI). It must be noted here that the same MD simulations indicated above were performed for models containing the CTA species. Analysis of the MD production runs shows that these systems always equilibrate with the CTA molecule adsorbed on one of the metal slabs. Even at the shortest separation, no bridges were observed in those simulations. This finding reinforces the idea of the importance of both ammonium groups to make possible the formation of bridges between the metal slabs. Additional simulations performed with more B<sub>20</sub> units (between 5 and 15) confirm that some B<sub>20</sub> molecules tend to be interacting between both metallic slabs at distances between 20 and 25 Å. However, the number of bridges is limited because the quaternary ammonium heads groups must be accommodated between other B<sub>20</sub> molecules with their alkyl chains adsorbed on the gold surface (Figure 3B and Figure S9–11 in the SI). On the other hand, MD runs with even more B<sub>20</sub> units (25 to 50) show a predominance of B<sub>20</sub> aggregation or formation of superposed layers on the surfaces (Figure S12 in the SI). From all of the above, it can be concluded that, on very dilute systems where most of the B<sub>20</sub> molecules are mainly adsorbed on the metallic surface, some B<sub>20</sub> molecules can adopt configurations that provide a bridging union between the metallic nanoparticles.

## 2.3. SERS Performance of B<sub>20</sub>-Induced AuSph Assemblies

So far, the results for the B<sub>20</sub>-induced AuSph assembly (noted as B<sub>20</sub>-AuSph) showed that the process was highly reproducible and that the B<sub>20</sub>-AuSph presented relatively long-term stability. Both features were identified as critical points for high-performance colloidal SERS sensor fabrication. Therefore, this system (B<sub>20</sub>-AuSph) was investigated for the development of a portable SERS approach for rapid sensing and quantification of drugs in aqueous solutions with a compact Raman device.

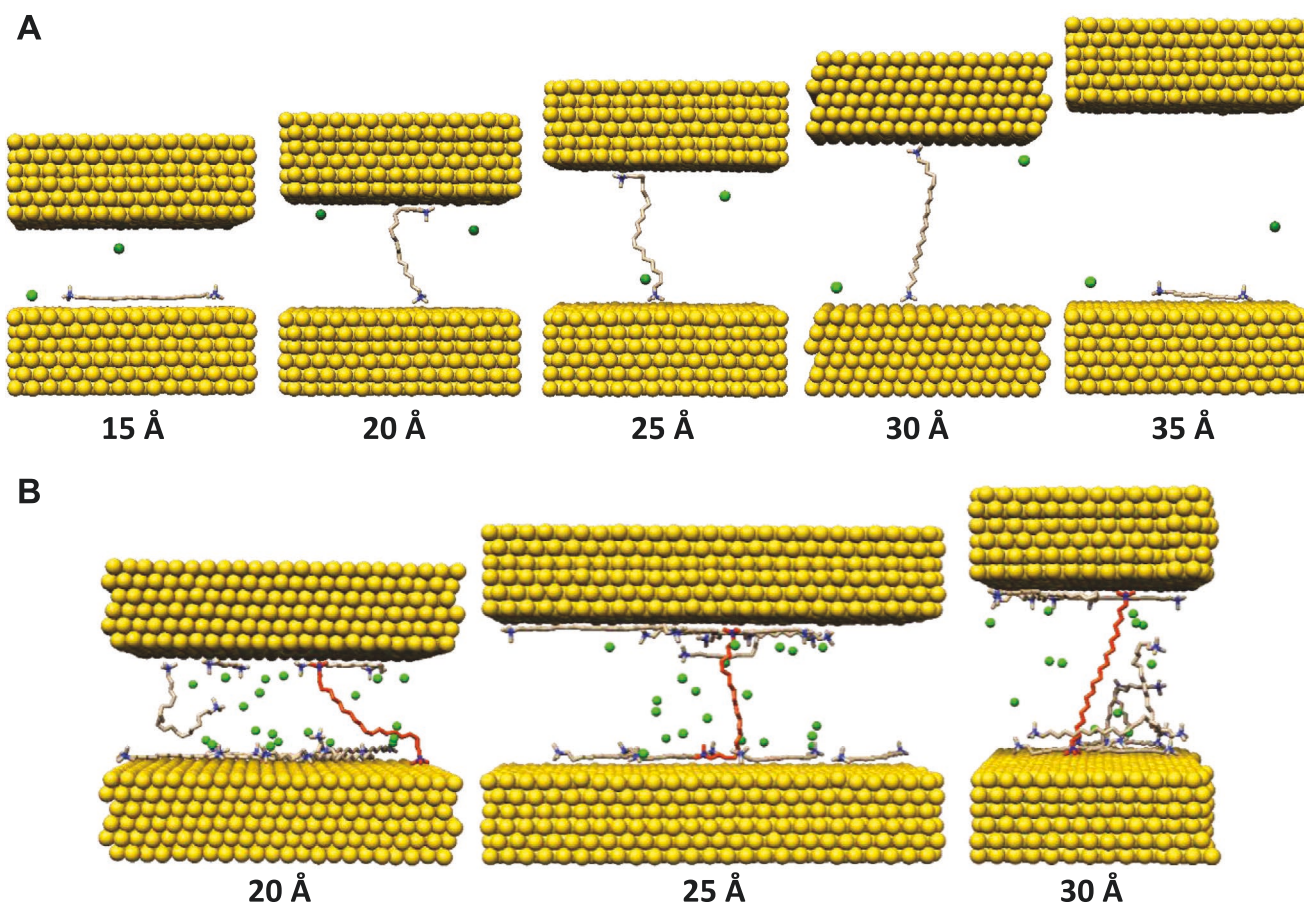


**Figure 3.** MD simulations were performed for two Au slabs containing B<sub>20</sub> molecules. A,B) Snapshots of the resulting MD simulation containing 1 (A) and 10 (B) B<sub>20</sub> units in aqueous solution located between two Au(111) slabs separated at different distances, as indicated. The B<sub>20</sub> molecules forming bridges between Au surfaces are highlighted in orange. Green spheres are chloride counteranions added to the solution to assure electroneutrality. Water molecules are not shown for clarity.

Taking crystal violet (CV) as Raman target analyte (the characteristic Raman peaks and its assignment are shown in Figure S13 and Table S3 in the SI), we analyzed the SERS efficiency of the B<sub>20</sub>-AuSph using a portable Raman spectrophotometer. First, time-resolved SERS analysis of the AuSph assembly process was performed to optimize the measurement conditions and get the highest SERS efficiency. For this purpose, different amounts of B<sub>20</sub> were added to an aqueous solution containing AuSphs (0.5 mM in terms of Au<sup>0</sup>) and CV (10<sup>-6</sup> M). Thus, a B<sub>20</sub> concentration range from 10<sup>-8</sup> to 5 × 10<sup>-4</sup> M was tested. The corresponding time-resolved SERS analysis performed with a portable Raman equipped with a 785 nm laser is shown in Figure S14 in the SI. The kinetic analysis showed that upon the addition of B<sub>20</sub>, the SERS signal increases exponentially during the first minute till reaching a plateau in less than 5 min (Figure S14E, SI). As expected, the highest SERS signals were achieved for the B<sub>20</sub> concentrations (10<sup>-6</sup> to 10<sup>-4</sup> M) (Figure S14F, SI) that triggered the AuSph assembly (Figure 2 and Figure S2 in the SI). Interestingly, the best SERS signal was obtained for a B<sub>20</sub> concentration of 10<sup>-6</sup> M, although the extension of the assembly was similar for 10<sup>-5</sup> M. This result could be ascribed to the available surface in the B<sub>20</sub>-AuSph assemblies since the presence of a higher

concentration of B<sub>20</sub> could prevent analytes from adsorbing at the formed hot spot. Finally, the SERS time-resolved analysis also indicated the long-term stability of the AuSph assemblies since the maximum SERS signal remained constant even 10 min after the B<sub>20</sub> addition. Based on these results, SERS analysis was always performed 5 min after adding a B<sub>20</sub> concentration of 10<sup>-6</sup> M.

Next, we evaluated the limit of detection (LOD) of CV with the colloidal B<sub>20</sub>-AuSph sensing platform. Therefore, AuSph assembly was performed by adding B<sub>20</sub> (10<sup>-6</sup> M) to AuSph colloids containing different CV concentrations (10<sup>-6</sup> to 10<sup>-10</sup> M). The SERS analysis of the samples 5 min after the B<sub>20</sub> addition showed that the characteristic signals of CV were distinguishable up to concentrations as low as 1 nM (Figure 4A). However, other signals corresponding to AuSph nanoparticles were also evidenced, which could interfere with analyte detection at low concentrations. Therefore, to perform a more robust data analysis for the accurate identification and quantification of the analyte, we performed PCA to the data set.<sup>[22]</sup> PCA transforms the data set,  $x$ , onto a new coordinate system,  $x_i$ , where the greatest variance by any data projection lies on the first principal component, the second greatest variance on the second coordinate, and so on.

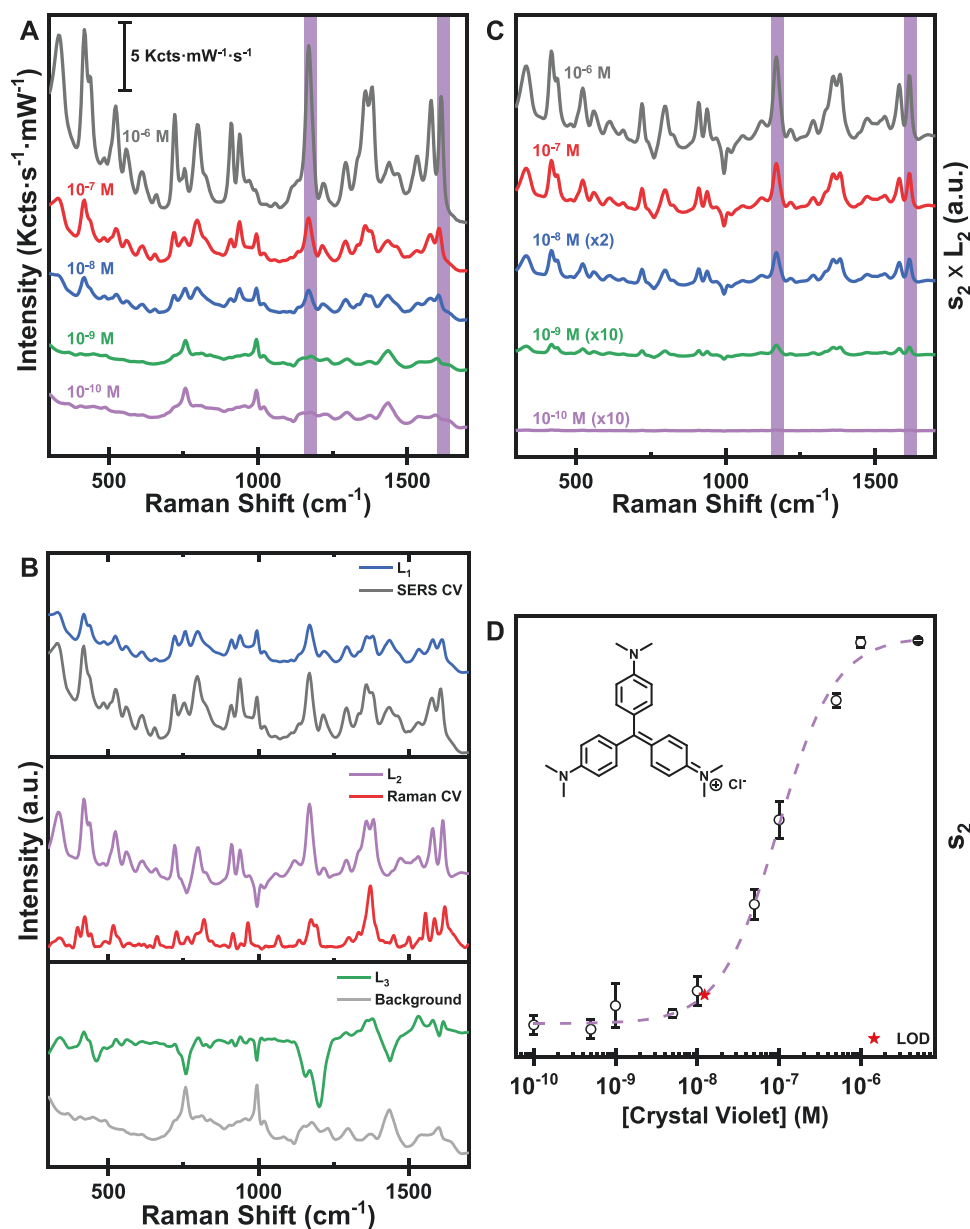


**Figure 4.** PCA analysis of the surface-enhanced Raman scattering (SERS) detection of crystal violet (CV). A) SERS spectra obtained for different CV concentrations ranging from 10<sup>-10</sup> M to 10<sup>-6</sup> M. The spectra were acquired with a time of acquisition of 30 s and a laser power of 257 mW. B) Principal component analysis (PCA) loading plots of the first three principal components (L<sub>1</sub>, L<sub>2</sub>, and L<sub>3</sub>) as indicated. The SERS spectra of B<sub>20</sub>-AuSph dispersion with and without CV (SERS CV and background, respectively) and the Raman spectrum of CV were included for better comparison. C) Isolated-SERS signal of CV for different molecule concentrations (10<sup>-10</sup> M to 10<sup>-6</sup> M) obtained from the product of scores by loading of the second component (s<sub>2</sub> × L<sub>2</sub>). D) Plot of s<sub>2</sub> as a function of the CV concentration. The error bars represent the standard deviation from three independent experiments. The dashed line represents the fit to a Langmuir-Hill isotherm model.

$$x = \sum x_i \quad (1)$$

This new coordinate system is decomposed into two sets of matrices as follows

$$x_i = s_i L_i \quad (2)$$

where s<sub>i</sub> is the score (the weight associated with each spectrum) and L<sub>i</sub> is the loading (a set of spectral components).

The great advantage of applying PCA to our system is that the loading of each component might be related to the isolated SERS signals of the different molecules contributing to the total spectrum. Figure 4B shows the loadings of the first three components (L<sub>1</sub>, L<sub>2</sub>, and L<sub>3</sub>) obtained via PCA analysis of the data set from Figure 4A. L<sub>1</sub> represents the most remarkable similarities among the entire data set; as shown in Figure 4B (upper panel), L<sub>1</sub> resembles the SERS spectrum of samples. The SERS spectrum of AuSph containing 10<sup>-6</sup> M B<sub>20</sub> and 10<sup>-6</sup> M

CV was included in Figure 4B (top) for better comparison. Besides,  $L_2$  (Figure 4B (center)) could be assigned with the CV since the  $L_2$  plot showed remarkable similarities with the Raman spectrum of CV (also included in the graph). Therefore, the second principal component could be used for the detection/identification of the molecule of interest. In fact, calculating the product  $s_2 \times L_2$  from the PCA analysis of the data set from Figure 4A could reconstruct the concentration-dependent relationship of the SERS spectrum of CV (Figure 4C). Figure 4D shows  $s_2$  values as a function of CV concentration. These data fitted very well to a Langmuir-Hill isotherm,

$$s_2 = A + \frac{(B - A) \cdot [\text{analyte}]^n}{k^n + [\text{analyte}]^n} \quad (3)$$

where A and B are constants representing the start and end value of the data set, respectively,  $k$  is the dissociation constant,  $n$  is the Hill coefficient, and [analyte] is the analyte concentration.

The good fitting of the experimental data to Equation (3) indicated the possibility of performing quantification analysis in a relatively wide CV concentration range. Finally, the LOD was estimated following the IUPAC recommendations, multiplying by three the standard deviation obtained from 10 independent measures of the blank and interpolating the value in the Langmuir-Hill Equation.<sup>[23]</sup> The obtained LOD value was  $1.23 \times 10^{-8}$  M.

## 2.4. SERS Detection of Drugs

To confirm the versatility of the proposed approach, the SERS-based sensing capabilities of the B<sub>20</sub>-AuSph were evaluated for a range of different drugs. Thus, two beta-blocker drugs (propranolol and atenolol) and four analgesics (benzocaine, ibuprofen, acetylsalicylic acid, and acetaminophen) were selected (Figure S15–S20 and Tables S4–S9 in the SI contains the characteristics Raman peaks and its assignation for each molecule). For each drug, SERS sensing experiments similar

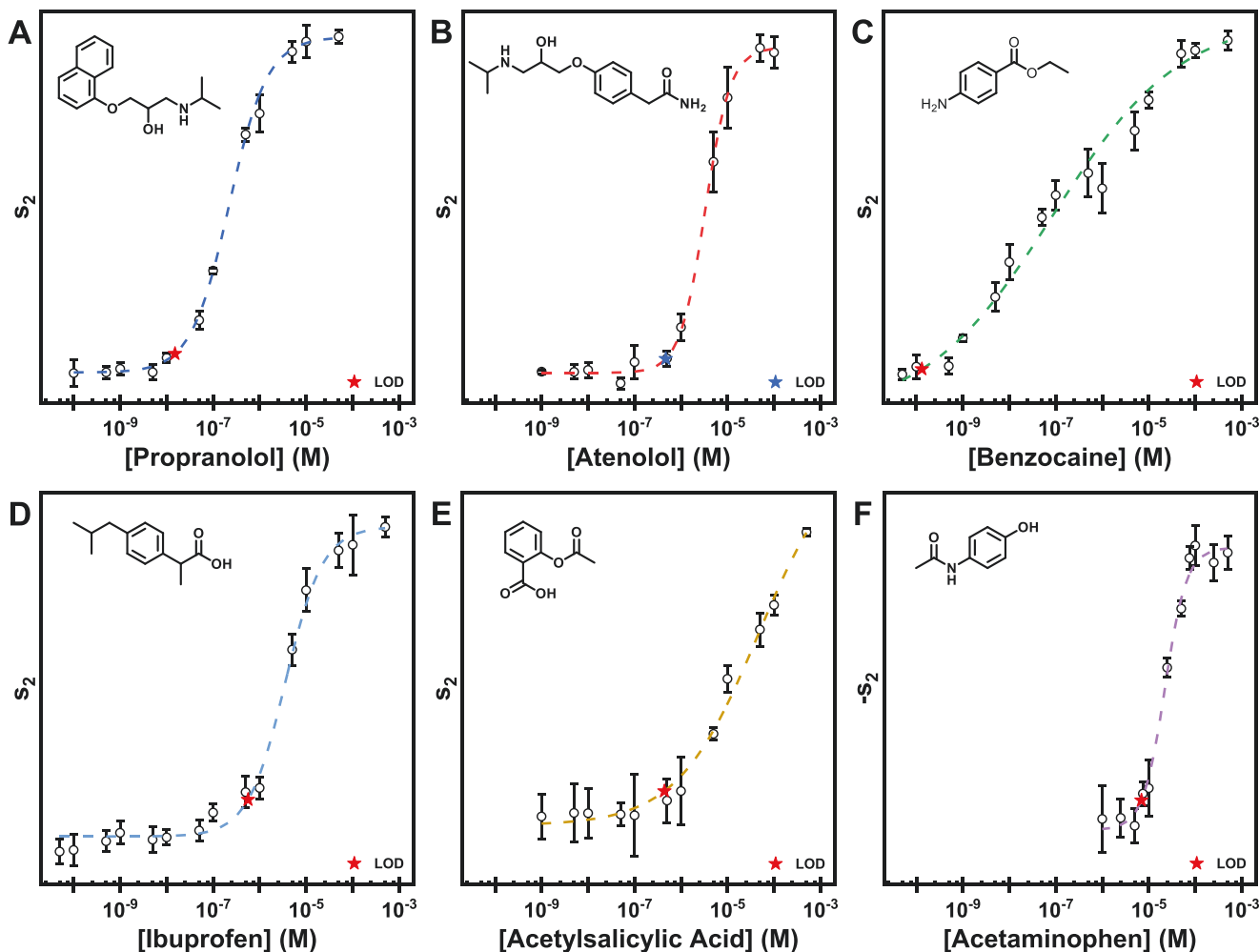


**Figure 5.** Relation between second component score ( $s_2$ ) and drug concentration. A–F) Representation  $s_2$  as a function of the drug concentration: Propranolol (A), atenolol (B), benzocaine (C), ibuprofen (D), acetylsalicylic acid (E), and acetaminophen (F). The error bars represent the standard deviation from three independent experiments. The dashed line represents the best fit to a Langmuir-Hill isotherm model.

**Table 1.** Obtained Langmuir-Hill coefficients and limit of detection for the different analytes.

Analyte	Langmuir-Hill coefficients			LOD [M]
	<i>K</i>	<i>n</i>	<i>R</i> <sup>2</sup>	
Crystal violet	$(9.6 \pm 1.6) \times 10^{-8}$	$1.23 \pm 0.16$	0.99831	$1.23 \times 10^{-8}$ M
Propranolol	$(22.1 \pm 0.8) \times 10^{-8}$	$1.06 \pm 0.04$	0.99923	$1.51 \times 10^{-8}$ M
Atenolol	$(3.3 \pm 0.5) \times 10^{-6}$	$1.59 \pm 0.20$	0.99570	$4.70 \times 10^{-7}$ M
Benzocaine	$(8.5 \pm 3.8) \times 10^{-8}$	$0.31 \pm 0.05$	0.99404	$1.32 \times 10^{-10}$ M
Ibuprofen	$(3.6 \pm 0.6) \times 10^{-6}$	$1.08 \pm 0.14$	0.99264	$5.65 \times 10^{-7}$ M
Acetylsalicylic acid	$(4.6 \pm 2.4) \times 10^{-5}$	$0.50 \pm 0.09$	0.99652	$4.38 \times 10^{-7}$ M
Acetaminophen	$(2.2 \pm 0.2) \times 10^{-5}$	$1.85 \pm 0.32$	0.99652	$6.94 \times 10^{-6}$ M

to those for CV were performed for concentrations ranging from  $10^{-10}$  to  $10^{-4}$  M. Figure S21 in the SI shows the SERS spectra recorded for the different drugs. Like for CV,  $L_2$  and  $s_2$  were obtained through PCA analysis for the drug sensing (Figures S22 and S23 in the SI). Subsequently, the  $s_2$  values were plotted versus the concentration for each drug and fitted to the Langmuir-Hill isotherm (Equation (3)). As shown in **Figure 5**, the experimental data fit very well regardless of the drug, obtaining *n* and *k* (**Table 1**). The values of *k* varied from  $8.45 \times 10^{-8}$  for benzocaine to  $4.59 \times 10^{-4}$  for acetylsalicylic acid. The relatively large variation in this constant could be ascribed to the differences in drug solubilities and the drug-gold interaction. Additionally, the LOD of each drug was estimated by interpolating in the Langmuir-Hill fitting the value of three times the standard deviation averaged from 10 independent measurements of the blank (Table 1).<sup>[23]</sup> Interestingly, the estimated LOD for the two beta-blocker drugs, propranolol, and atenolol ( $1.5 \times 10^{-8}$  and  $4.70 \times 10^{-7}$  M, respectively) were comparable with the best LODs reported in the literature for SERS-based measurements (see **Table 2**). In the case of the analgesics, the LODs were similar to others previously reported or even better. For instance, LOD for benzocaine was  $1.32 \times 10^{-10}$  M, the lower value reported for SERS-based measurements to the best of our knowledge. Still, it should be pointed out that in most of the previously published works, a more complex SERS substrate was proposed, or even a pretreatment or extraction process of the analyte was required. Finally, it must be highlighted that a linear range in a relevant concentration range was observed for all the studied drugs, indicating the possibility of performing quantitative analysis.

## 2.5. Multiplexed Detection Using Deep Learning

Ralbosvky and Lednev,<sup>[38]</sup> in a comprehensive review, exposed that chemometrics techniques using artificial intelligence are gaining prominence in recent years and, when combined with Raman spectroscopy, become a powerful method for diagnostics and sensing. These promising new methods are based on deep learning architectures, where Convolutional Neural Networks (CNNs) stand out in a range of computer vision tasks. ResNets<sup>[39]</sup> are state-of-the-art CNNs that show better results in training convergence and classification stability of Raman spectra<sup>[40]</sup> due to their architecture allowing to build deeper

**Table 2.** Limit of detection reported for the different drugs employing SERS.

Analyte	Sensing platform	LOD	Ref
Crystal violet	B <sub>20</sub> -AuSph	$1.23 \times 10^{-8}$ M	This work
	Ordered Au nanorods arrays	$5 \times 10^{-9}$ M	[24]
	AuSph printed on chromatographic paper	$1 \times 10^{-10}$ M	[25]
Propranolol	Octahedral Au NPsuper-crystal	$1 \times 10^{-19}$ M	[26]
	B <sub>20</sub> -AuSph	$1.51 \times 10^{-8}$ M	This work
	Aggregated Ag nanoparticles	$7.79 \times 10^{-9}$ M	[27]
Atenolol	Sandwich nanostructure of GO/MIPs hybrids and Ag NPs	$1 \times 10^{-11}$ M	[28]
	B <sub>20</sub> -AuSph	$4.70 \times 10^{-7}$ M	This work
	3D network of meso-Au NPs	$3.4 \times 10^{-8}$ M	[29]
Benzocaine	Ag colloids combined with solvent micro-extraction	$0.1 \mu\text{g mg}^{-1}$	[30]
	Ag NPs	$8.9 \times 10^{-6}$ M	[31]
	B <sub>20</sub> -AuSph	$1.32 \times 10^{-10}$ M	This work
Ibuprofen	Superlattice array of plasmonic nanocubes	$6.05 \times 10^{-7}$ M	[32]
	AuSph film over 107nm polystyrene spheres	$4.3 \times 10^{-7}$ M	[33]
	B <sub>20</sub> -AuSph	$5.65 \times 10^{-7}$ M	This work
Acetylsalicylic acid	Lipophilic multibranching Au NPs	$1 \times 10^{-8}$ M	[34]
	Superlattice array of plasmonic nanocubes	$4.85 \times 10^{-5}$ M	[32]
	$\beta$ -cyclodextrin stabilized Ag NPs	$1 \times 10^{-4}$ M	[35]
Acetaminophen	B <sub>20</sub> -AuSph	$4.38 \times 10^{-7}$ M	This work
	3D network of meso-Au NPs	$2.8 \times 10^{-6}$ M	[29]
	Superlattice array of plasmonic nanocubes	$5.55 \times 10^{-5}$ M	[32]
Acetaminophen	Ag substrate laser-induced	$1.77 \times 10^{-7}$ M	[36]
	B <sub>20</sub> -AuSph	$6.94 \times 10^{-6}$ M	This work
	Superlattice array of plasmonic nanocubes	$6.62 \times 10^{-5}$ M	[32]
	Au NPs on an anodic aluminium oxide filter	$1 \times 10^{-5}$ M	[37]

networks. ResNets have been recently used for pathogen identification and antibiotic susceptibility testing,<sup>[41]</sup> brain tumor classification,<sup>[42]</sup> or component identification in Raman spectra of mixtures.<sup>[43]</sup>

Next, we investigated if our SERS sensing platform could identify a binary mixture of two analytes when combined with deep learning tools. We chose a mixture of ibuprofen and benzocaine in water as a model system. Thus, different mixtures of the two analgesics (expressed in terms of the percentage concentration of ibuprofen with respect to the total analgesic concentration) were prepared, keeping the total analgesic concentration to  $10^{-6}$  M. Figure S24, SI, shows the SERS spectra of the different ibuprofen-benzocaine mixtures. Two different models were employed: MNN and ResNet. The data set corresponding to each ibuprofen-benzocaine mixture was separately used to train and test both deep learning models. For the



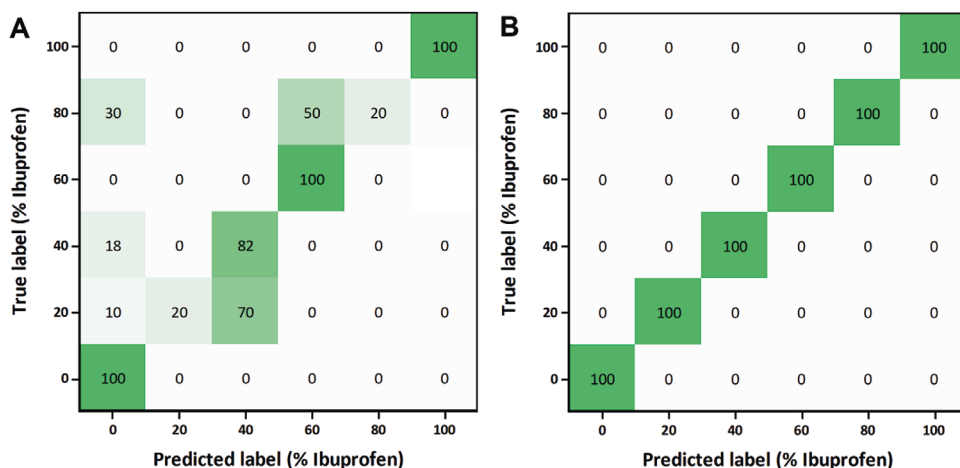


**Figure 6.** Confusion matrices show the prediction percentage of different ibuprofen-benzocaine mixtures. A) MNN and B) ResNet deep learning architectures were applied to classify the percentage of ibuprofen in the analgesic mixture. The total concentration of analgesics in the mixtures was  $10^{-6}$  M, and they were expressed in terms of the percentage concentration of ibuprofen with respect to the total analgesic concentration. At least ten different samples of each molar ratio were predicted.

training process, 70% of the data set, randomly chosen, was used (see experimental section and Section 4 in the SI for further details). The test phase was performed by introducing the remaining 30% of the data set as inputs to check if the models could predict the composition of the corresponding mixture. Thus, we found out that the MNN, composed of 14 dense layers, wasn't powerful enough since it showed 72.2% prediction accuracy (see confusion matrix in **Figure 6A**). A ResNet model consisting of 5 residual blocks was employed to improve these results. This convolutional neural network performed various operations such as Convolutions, Max-pooling, ReLU, and Batch-normalization (see experimental information for further details) to find unique patterns for each ibuprofen-benzocaine mixture. After performing the training process, similar to the MNN model, the test phase revealed that the ResNet model was able to predict the composition of the mixture with 100% accuracy (**Figure 6B**). An extensive description of the data visualization, pre-processing, model building, and evaluation of model loss and accuracy are described in the experimental section.

## 2.6. Millifluidic SERS Sensing

The excellent sensing capabilities of the  $B_{20}$ -AuSph motivated us to investigate the possibility of integrating this sensing platform within a polydimethylsiloxane (PDMS) millifluidic chip. Therefore, a PDMS chip was designed with two inlets converging in a pre-mixer Y-shaped connection, a sinusoidal type mixer, and a measuring chamber (see **Figure 7A**).<sup>[44,45]</sup> The dimensions of the millifluidic channel were  $1 \times 1 \text{ mm}^2$  in cross-section and  $\approx 8 \text{ cm}$  in length; while the measuring chamber was  $2 \times 2 \times 1 \text{ mm}^3$  (length  $\times$  width  $\times$  height); therefore, the total volume was ca  $100 \mu\text{L}$ . Interestingly, the template used for the chip fabrication was printed in a 3D printer employing ABS polymer with a cost of  $\approx 0.3$  \$, and it was replicated in a PDMS slab ( $6 \times 3 \times 0.5 \text{ cm}^3$ , length  $\times$  width  $\times$  height, and  $\approx 10$  g) by less than 1 \$ per chip.

First, we studied the  $B_{20}$ -AuSph in the PDMS millifluidic chip. To test the reproducibility, we performed 15 different

experiments, and the resulting  $B_{20}$ -AuSph were evaluated by UV-vis-NIR spectroscopy. As shown in **Figure S27** in the SI, using a millifluidic chip gave rise to highly uniform  $B_{20}$ -AuSph (as revealed the low variability of the optical properties), improving the reproducibility achieved in a cuvette

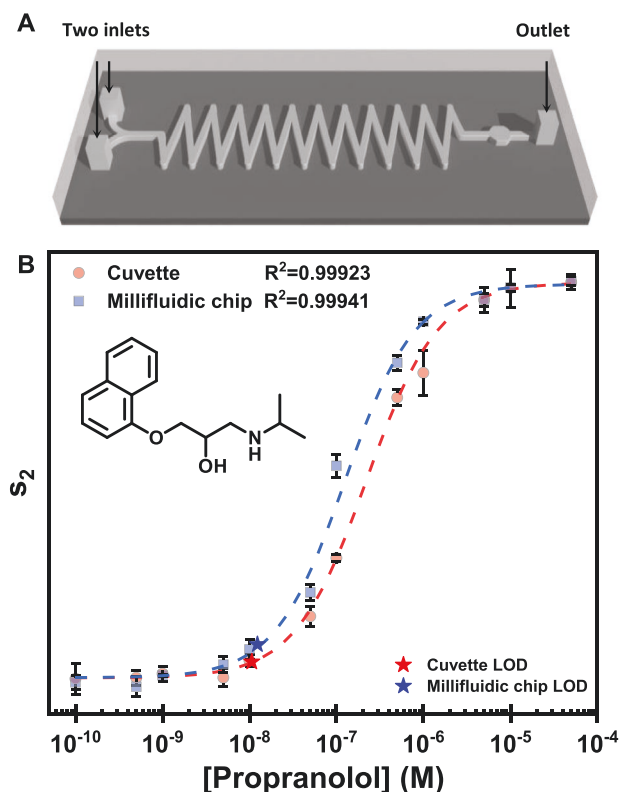


**Figure 7.**  $B_{20}$ -AuSph millifluidic chip for SERS sensing of propranolol. A) Schematic illustration of the millifluidic chip to perform  $B_{20}$ -AuSph based sensing. B) Representation of  $S_2$  as a function of the concentration of propranolol for experiments performed in a cuvette (red) and in a millifluidic chip (blue).

(Figure S5 in the SI). Interestingly, the higher extinction ratio  $\text{Ext}_{780}/\text{Ext}_{540}$  obtained in a millifluidic chip (Figure S25C, SI) indicated a higher density of hot spots than that obtained in a cuvette. Additionally, the AuSph assembly kinetic performed in a millifluidic chip is faster than in the case of a cuvette. While the equilibrium of the AuSph assembly was reached in less  $\approx 5$  min for cuvette experiments (Figure S2G, SI), it was  $\approx 10$  s (for a flow rate of  $\approx 5 \mu\text{L s}^{-1}$ ) in the millifluidic chip.

Next, we evaluated the efficiency of this millifluidic sensing platform by performing SERS experiments with propranolol for concentrations ranging from  $10^{-10}$  to  $10^{-4}$  M, and we compared the results with those obtained previously in a cuvette. Figure S28 in the SI shows representative SERS spectra recorded for the different propranolol concentrations. Like in the previous case performed in a cuvette,  $s_2$  was obtained through PCA analysis and plotted versus the propranolol concentration. Figure 7B shows the  $s_2$  plots corresponding to millifluidic and cuvette platforms and their corresponding fittings to the Langmuir-Hill isotherm (Equation (3)). The experimental data fitted very well in both platforms, achieving similar LODs ( $1.06 \times 10^{-8}$  M vs  $1.24 \times 10^{-8}$  M for cuvette and millifluidic chip, respectively). Although no improvement in the LOD was observed using the millifluidic platform, this result demonstrated the practical applicability of the chip to induce the bolaform surfactant-promoted AuSph assembly without losing any SERS capabilities.

Finally, we study the reusability of the millifluidic PDMS chip by performing multiple successive experiments and analyzing the background signal after each of them. It is essential to highlight that this analysis is very dependent on the concentration of the analyte employed. For this reason, we decided to use the highest concentration in the linear range of propranolol,  $10^{-5}$  M. After each measure, the chip was washed with 2 mL of 10 mM CTAB followed by 2 mL of water. As shown in Figure S29 in the SI, the characteristic SERS signals of propranolol completely disappeared after the different washing cycles. Therefore, the chip could be reused at least ten times without altering its performance, which could reduce the cost of the chip by at least 10 times.

Additionally, we investigated the influence of the solution pH in the performance of the  $\text{B}_{20}$ -AuSph millifluidic chip. As shown in Figure S30 in the SI, the sensor exhibits a similar sensitivity in a pH range from 2.8 to 11.2, being in all cases the LOD at the nanomolar range. As shown in Figure S31 in the SI, experiments performed with tap water or river water showed a decrease in the aggregation, so the  $\text{B}_{20}$ -AuSph needs to be studied and optimized as a function of the matrix.

### 3. Conclusions

We demonstrated that the surface modification of citrate-stabilized AuSphs by the adsorption of the bolaform surfactant  $\text{B}_{20}$  led to the highly reproducible and controllable assembly of the nanoparticles in a broad surfactant concentration range ( $10^{-4}$ – $10^{-7}$  M). The decrease of the surface charge combined with the bridging effect, both promoted by  $\text{B}_{20}$ , were hypothesized as the key points governing the assembly. Interestingly, MD simulations supported the bridging effect of the  $\text{B}_{20}$  by showing the preferential bridging of surfactant monomers

when two adjacent Au(111) slabs were separated from each other between 20 and 25 Å. Using a portable Raman spectrometer, we also demonstrated the excellent SERS capabilities of the colloidal  $\text{B}_{20}$ -AuSph assemblies to detect different beta-blockers and analgesic drugs in the nanomolar regime. Additionally, we showed that a state-of-the-art CNN, such as a ResNet model, was a robust architecture for finding patterns in Raman spectra, allowing a 100% accuracy in classifying the concentration of different binary mixtures. Finally, the colloidal approach was successfully implemented in a millifluidic chip enabling the automation of the whole process and improving the sensor's performance in terms of speed, reliability, and reusability without affecting its sensitivity.

### 4. Experimental Section

**Materials:** Acetaminophen ( $\text{C}_8\text{H}_9\text{NO}_2$ ,  $\geq 99.9\%$ ), Acetylsalicylic acid ( $\text{C}_9\text{H}_8\text{O}_4$ ,  $\geq 98\%$ ), Atenolol ( $\text{C}_{14}\text{H}_{22}\text{N}_2\text{O}_3$ ,  $\geq 98\%$ ), Benzocaine ( $\text{C}_9\text{H}_{11}\text{NO}_2$ ,  $\geq 99\%$ ), propranolol ( $\text{C}_{16}\text{H}_{21}\text{NO}_2$ ,  $\geq 99\%$ ), Sodium citrate tribasic dihydrate ( $\text{Na}_3\text{C}_6\text{H}_5\text{O}_7 \cdot \text{H}_2\text{O}$ ,  $\geq 98\%$ ) and were purchased from Sigma-Aldrich. Ibuprofen ( $\text{C}_{13}\text{H}_{18}\text{O}_2$ , 99%), and hexadecyltrimethylammonium bromide ( $\text{C}_{19}\text{H}_{42}\text{BrN}$ ,  $\geq 99\%$ ) were acquired from Acros Organics. Ethanol ( $\text{C}_2\text{H}_6\text{O}$ ,  $\geq 99.9\%$ ) was supplied by Scharlab, Hydrogen tetrachloroaurate (III) hydrate ( $\text{HAuCl}_4 \cdot 3\text{H}_2\text{O}$ , 99.9%) was purchased by Alfa-Aesar, poly(dimethylsiloxane) (PDMS, Sylgard-184) by Dow-Corning, and Crystal Violet ( $\text{C}_{25}\text{N}_3\text{H}_{30}\text{Cl}$ , 90%) by Analema. All chemicals were used without further purification. Milli-Q grade water was used in all the preparations.

**Characterization:** UV-vis-NIR extinction spectra of gold spheres nanoparticles were measured with a Cary 8454 spectrophotometer (Agilent). Quartz cuvettes with an optical path length of 1.0 cm were used. Transmission electron microscopy (TEM) images were obtained with a JEOL JEM 1010 transmission electron microscope operating at an acceleration voltage of 100 kV. Scanning electron microscopy (SEM) images were acquired using a JEOL JSM-6700F FEG scanning electron microscope operating at an acceleration voltage of 15.0 kV in secondary-electron imaging (SEI) mode.  $\zeta$ -Potential and hydrodynamic diameter was determined using a Zetasizer Nano S (Malvern Instruments, Malvern UK).

Raman characteristic peaks of the different molecules were characterized by directly measuring the solid powder of each molecule using a Renishaw InVia Reflex system. The spectrograph used a high-resolution grating (1200 grooves per cm) with additional band-pass filter optics, a confocal microscope, and a 2D-CCD camera. Laser excitation was carried out employing a 50x objective (N.A. 0.75) with an excitation wavelength of 785 nm (33.9 mW) with an acquisition time of 10 s and five accumulations. The spectra were acquired using WiRE Software v. 4.3 (Renishaw, UK). All SERS measurements were carried out in a QEPPro (Ocean Insight) Raman spectrometer equipped with a back-thinned FFT-CCD detector. Laser excitation was carried out at 785 nm (257 mW) through a Raman probe BAC102 employing acquisitions times of 30 s. All the spectra were acquired without treatment using OceanView Software v. 2.0.7 (Ocean Insight).

**Synthesis of Gold Spheres:** Gold nanospheres (AuSphs) were synthesized according to a previously reported seed-mediated growth synthetic method.<sup>[20]</sup> 150 mL of trisodium citrate dihydrate 2.2 mM was placed in a 250 mL three-necked round-bottomed flask with a magnetic stirring bar and heated until boiling. Then under vigorous stirring, 1 mL of an aqueous solution of 25 mM  $\text{HAuCl}_4 \cdot 3\text{H}_2\text{O}$  was added in a one-shot, and the solution was kept at 100 °C for 15 min. A color change was observed during this time. First, a black color appears that slowly changes to a soft reddish-pink color indicating the formation of tiny nanoparticles that act as seeds. After that, the solution was cooled to 90 °C, and to overgrowth, the seeds obtained, 1 mL of 25 mM  $\text{HAuCl}_4$  solution was quickly added to the solution twice with a 30 min interval between additions. After 30 min from the last addition, 55 mL of solution

was retired from the round-bottomed flask to a vial that immediately was put on an ice-water bath to stop the nanoparticle growth. Then 53 mL of Milli-Q water and 2 mL of 60 mM sodium citrate dihydrate were added to the remaining solution in the round-bottomed flask. After the solution reached 90 °C again, 1 mL of 25 mM aqueous solution of  $\text{HAuCl}_4 \cdot 3\text{H}_2\text{O}$  was added in a one-shot to the solution three times with a 30 min interval between additions. Then, another 55 mL of solution was substrated like in the previous case, followed by the addition of water, sodium citrate, and three additions of gold salt. This process was repeated several times until obtaining the desired nanoparticle diameter.

The AuSph colloids were washed by centrifugation (3500 rpm  $\times$  40 min), then the supernatant was discarded, and the pellet was redispersed in water. A second centrifugation step was carried out (3000 rpm  $\times$  40 min) but the pellet was concentrated to a final gold concentration of 6.95 mM in terms of  $\text{Au}^0$  with water. Their average diameter and morphology were confirmed by TEM and SEM.

**Synthesis of Bolaform ( $B_{20}$ ):** Bolaform molecule,  $B_{20}$ , was synthesized from the corresponding  $\alpha, \alpha'$ -dibromide. 1,20-dibromoeicosane was obtained from 11-bromoundecanoic acid by Kolbe's electrolysis of the  $\alpha$ -bromo carboxylic acid in methanol.<sup>[46]</sup> The dibromide (5 mmol) and anhydrous trimethylamine (10 mmol) were dissolved in 50 mL of acetone and heated until boiling under reflux for 96 h. The material obtained after removal of the solvent with a rotary evaporator was crystallized from ethanol-ether mixtures. The final product was characterized by NMR (Figure S32, Supporting Information),  $^1\text{H}$  NMR (400MHz,  $\text{D}_2\text{O}$ , ppm):  $\delta = 3.32$  (t, 4H), 3.11 (s, 18H), 1.80 (s, 4H), 1.34 (s, 4H) and 1.29 (s, 28H). The critical micelle concentration (CMC) was determined by conductivity measurements yielding a value of  $4.33 \times 10^{-3}$  M with a fraction of neutralized charge  $\beta$  of 0.59.

**$B_{20}$ -induced AuSph Assembly:** Different solutions of  $B_{20}$  were prepared in water (from  $10^{-1}$  M to  $10^{-6}$  M), and 20  $\mu\text{L}$  of these solutions were added to a volume of 1980  $\mu\text{L}$  of AuSph 0.505 mM (in terms of  $\text{Au}^0$ ). The different mixed solutions with a final concentration of gold of 0.5 mM and final  $B_{20}$  concentrations between  $10^{-3}$  M and  $10^{-8}$  M were manually shaken for 5 s. Then the aggregation process was followed by UV-vis-NIR spectrophotometry. A new series of mixtures with different final  $B_{20}$  concentrations between  $10^{-1}$  and  $10^{-10}$  M were prepared again to measure  $\zeta$ -Potential and the hydrodynamic diameter after 5 min of reaction. As a control experiment, the same protocol was reproduced, but this time, AuSphs were mixed with different concentrations of CTAB to characterize UV-vis,  $\zeta$ -Potential, and DLS.

**Millifluidic Chip Fabrication:** First, the desired millifluidic chip mask was designed using Blender software version 2.90.1 (www.blender.org, Netherlands) and exported as .stl format. However, any other 3D modeling/CAD software that can export models in a .stl file format could be employed to obtain the desired design. The optimized chip design consists of two inlets that converge in a Y-shaped pre-mixer, a mixing area, a measuring chamber, and an outlet (Figure 7A). The mixer section consists of a sinusoidal shape with 10 curves. All the millifluidic channels have a square cross-section of  $1 \times 1$  mm<sup>2</sup>, resulting in a total linear length of  $\approx 8$  cm. For 3D printing, the .stl file was loaded into the Ultimaker Cura software version 4.12.1 (Netherlands), and printed using the Creality Ender 3 (CREALITY, China) 3D printer. The devices were printed using acrylonitrile butadiene styrene (ABS), employing a nozzle of 0.4 mm at 235 °C.

The obtained mask was replicated by curing a mixture of PDMS monomer and curing agent (10:1 w/w) for 6 h at 50 °C. The resulting PDMS slab was peeled off and punched to create the inlets and outlet. Finally, it was deposited on an uncured thin PDMS film of  $\approx 200$   $\mu\text{m}$  that was previously prepared by spin-coating (1000 rpm for 10 s) and cured at 60 °C for 2 h.

**In-chip  $B_{20}$ -AuSph:** In a millifluidic chip were infiltrated two solutions employing a constant flow rate of  $\approx 5$   $\mu\text{L s}^{-1}$  simultaneously. One of the solutions was a mixture of AuSph (1 mM) and the desired analyte in different concentrations (from  $2 \times 10^{-4}$  to  $2 \times 10^{-10}$ ) while the other contained the surfactant  $B_{20}$  with a concentration of  $2 \times 10^{-6}$  M. In the mixing area the fast color change of the nanoparticles from pink to purple-grey was observed immediately. To reuse the channel, 2 mL of CTAB 10 mM followed by another 2 mL of water were passed through the chip.

**Molecular Dynamic Simulations:** MD simulations were performed using GROMACS (version 2021.3)<sup>[47]</sup> and the CHARMM36 force field.<sup>[48]</sup> The Lennard-Jones parameters for gold were those reported by Heinz et al.,<sup>[49]</sup> which have been proven to provide good descriptions for systems adsorbed on gold surfaces. The parameters for  $B_{20}$  were generated with the CGenFF program<sup>[50]</sup> and could be used without further refinement. The parameters for CTA and the chloride anions added to the solution to maintain electroneutrality were also those included in the CHARMM36 force field. Additional details of the models employed in the MD simulations are provided in Section 2 in the SI.

**Deep Learning:** Two different algorithms were applied to the SERS data set from six different ibuprofen-benzocaine mixtures. The composition of the analyzed mixtures was 0, 20, 40, 60, 80, and 100 % of ibuprofen with respect to the total concentration of analgesic ( $10^{-6}$  M) (Figure S24, Supporting Information). The obtained 180 SERS spectra, 30 per mixture, were used for this classification problem. In turn, each sample was composed of a one-dimensional array of 1023 positions representing the spectral range from 1 to 2807  $\text{cm}^{-1}$ . First, we pre-processed the whole data to reduce some parts of the Raman shift that we consider less relevant. Thus the spectral range of interest was fixed from 300 – 1800  $\text{cm}^{-1}$  after the pre-processing (Figure S25A, Supporting Information). Subsequently, a baseline correction data pre-processing, based on adaptive iteratively reweighted Penalized Least Squares (airPLS),<sup>[51]</sup> was applied to each sample independently to separate relevant spectroscopic signals from interference effects or remove background effects (Figure S25B, Supporting Information). The data set corresponding to each ibuprofen-benzocaine mixture (Figure S25C, Supporting Information) was separately used to train and test the deep learning models.

The first deep learning model built was a Multilayer Neural Network (MNN) composed of 14 dense layers. The reason for creating this network was to study whether a more traditional architecture could solve the current task.<sup>[52]</sup> MNN was trained for 350 epochs with the Adam optimizer and the categorical cross-entropy loss function. The training processes used 70% of the data, randomly chosen. Finally, a test phase, which consisted of introducing the remaining 30% of the samples as inputs, was performed to see if the models could predict to which mixture it belongs.

The second deep learning model was a ResNet model: a modern convolutional neural network capable of achieving high accuracy in image recognition problems.<sup>[40]</sup> Considering the SERS spectrum as a one-dimensional vector or image, a state-of-the-art deep learning architecture was implemented to solve the ibuprofen-benzocaine mixture classification problem. This convolutional neural network carried out various operations such as Convolutions, Max-pooling, and ReLU to find unique patterns for each mixture type.

- **Convolutions:** It consists of sliding a predefined filter (matrix/vector) with learnable parameters to detect features such as edges or convex shapes over the input data creating a feature map.
- **Max-pooling:** It reduces the number of parameters (computational cost). This operation reduces the resolution of the feature map, taking the largest value of a segment, but preserves the map features needed for classification.
- **ReLU (Rectified Linear Unit):** This widely used activation function calculates when a neuron should be activated.

Although these operations require a higher computational cost, this type of architecture is more appropriate for the detection of unique patterns in the spectra of each mixture. The central part of the ResNet model that was built comprises 5 residual blocks that perform these types of operations.

The ResNet model was trained for a total of 300 epochs with 32 kernels, Adam optimizer, and categorical cross-entropy loss function. Like MNN, the ResNet training processes used 70% of the data, randomly chosen. Figure S26 shows the evolution of the loss and accuracy of the ResNet model graphically during the training phase.

Finally, a test phase consisted of introducing the remaining 30% of the samples as inputs to see if the models can predict which mixture

it belongs to. The results of both architectures are shown in the confusion matrices represented in Figure 6. Also, the code is available on Github.

***B<sub>20</sub>-AuSph SERS Optimization:*** First, to optimize the B<sub>20</sub> concentration 445 μL of colloidal AuSphs (0.562 M in terms of Au<sup>0</sup>) and 50 μL of 10<sup>-6</sup> M CV were placed on a quartz cuvette (0.5 cm of optical path length). Then 5 μL of an aqueous B<sub>20</sub> solution was added and manually shaken for a few seconds. Experiments with B<sub>20</sub> concentrations ranging from 10<sup>1</sup> to 10<sup>-8</sup> M were carried out. The SERS spectra were recorded each 30 s employing a laser power of 257 mW with a time of acquisition of 10 s.

***In-Cuvette SERS Analysis of LOD:*** 445 μL of colloidal AuSphs (0.562 M in terms of Au<sup>0</sup>) and 50 μL of CV or drug at different concentrations (between 10<sup>-2</sup> and 10<sup>-9</sup> M) were mixed in a 0.5 cm quartz cuvette and then 5 μL of 10<sup>-4</sup> M B<sub>20</sub>. After 5 min, the SERS spectra were recorded employing a laser power of 257 mW with 30 s of acquisition time. All the concentrations were characterized by triplicate, and also 10 independent measurements of B<sub>20</sub>-AuSphs without any analyte were carried out.

***In-Chip SERS Measurements:*** Once the millifluidic chip is filled, SERS measurements were performed employing a laser power of 257 mW with a time of acquisition of 10 s. All experiments were characterized by triplicate. Moreover, 10 independent measurements of B<sub>20</sub>-AuSphs in the absence of any analyte were carried out as blanks.

## Supporting Information

Supporting Information is available from the Wiley Online Library or from the author.

## Acknowledgements

The authors acknowledge financial support from the European Innovation Council (Horizon 2020 Project: 965018—BIOCELLPHE) the MCIN/AEI/10.13039/501100011033 (grants PID2019-108954RB-I00 and PID2019-106960GB-I00 and FPI, BES-2017-081670) and FSE (“El FSE invierte en tu futuro”), the MEC of Spain (grant CTQ2017-84354-P), Xunta de Galicia/FEDER (grants GRC ED431C 2020/09 and GR 2007/085) and the European Regional Development Fund (ERDF). The authors thank Cesar Bolzoni Marciel for assisting with millifluidic devices design and 3D impression.

## Conflict of Interest

The authors declare no conflict of interest.

## Data Availability Statement

The data that support the findings of this study are openly available in zenodo.org at <https://doi.org/10.5281/zenodo.5806132>, reference number 5806132.

## Keywords

SERS, plasmonic nanoparticles, Au nanoparticles assembly, millifluidics, drug sensing, deep learning, ResNet

Received: December 28, 2021

Revised: March 11, 2022

Published online: April 3, 2022

- [1] J. Langer, D. Jimenez de Aberasturi, J. Aizpurua, R. A. Alvarez-Puebla, B. Auguie, J. J. Baumberg, G. C. Bazan, S. E. J. Bell, A. Boisen, A. G. Brolo, J. Choo, D. Ciialla-May, V. Deckert, L. Fabris, K. Faulds, F. J. Garcia de Abajo, R. Goodacre, D. Graham, A. J. Haes, C. L. Haynes, C. Huck, T. Itoh, M. Käll, J. Kneipp, N. A. Kotov, H. Kuang, E. C. le Ru, H. K. Lee, J.-F. Li, X. Y. Ling, et al., *ACS Nano* **2020**, *14*, 28.
- [2] D. Ciialla-May, X.-S. Zheng, K. Weber, J. Popp, *Chem. Soc. Rev.* **2017**, *46*, 3945.
- [3] G. Bodelón, I. Pastoriza-Santos, *Front. Chem.* **2020**, *8*, 478.
- [4] E. C. le Ru, P. G. Etchegoin, *MRS Bull.* **2013**, *38*, 631.
- [5] D. García-Lojo, S. Núñez-Sánchez, S. Gómez-Graña, M. Grzelczak, I. Pastoriza-Santos, J. Pérez-Juste, L. M. Liz-Marzán, *Acc. Chem. Res.* **2019**, *52*, 1855.
- [6] R. Pilot, R. Signorini, C. Durante, L. Orian, M. Bhamidipati, L. Fabris, *Biosensors* **2019**, *9*, 57.
- [7] J.-E. Park, Y. Jung, M. Kim, J.-M. Nam, *ACS Cent. Sci.* **2018**, *4*, 1303.
- [8] I. Szilagy, A. Sadeghpour, M. Borkovec, *Langmuir* **2012**, *28*, 6211.
- [9] K. A. Huynh, K. L. Chen, *Environ. Sci. Technol.* **2011**, *45*, 5564.
- [10] L. Guerrini, D. Graham, *Chem. Soc. Rev.* **2012**, *41*.
- [11] C. Ortiz, C. Caleman, *J. Phys. Chem. C* **2007**, *111*, 17442.
- [12] J.-W. Park, J. S. Shumaker-Parry, *J. Am. Chem. Soc.* **2014**, *136*.
- [13] M. Grzelczak, L. M. Liz-Marzán, R. Klajn, *Chem. Soc. Rev.* **2019**, *48*, 1342.
- [14] R. W. Taylor, T.-C. Lee, O. A. Scherman, R. Esteban, J. Aizpurua, F. M. Huang, J. J. Baumberg, S. Mahajan, *ACS Nano* **2011**, *5*, 3878.
- [15] S. J. Barrow, S. Kaseera, M. J. Rowland, J. del Barrio, O. A. Scherman, *Chem. Rev.* **2015**, *115*, 12320.
- [16] Q. An, G. Li, C. Tao, Y. Li, Y. Wu, W. Zhang, *Chem. Commun.* **2008**, 1989.
- [17] S. T. Jones, R. W. Taylor, R. Esteban, E. K. Abo-Hamed, P. H. H. Bomans, N. A. J. M. Sommerdijk, J. Aizpurua, J. J. Baumberg, O. A. Scherman, *Small* **2014**, *10*, 4298.
- [18] D. O. Sigle, S. Kaseera, L. O. Herrmann, A. Palma, B. de Nijs, F. Benz, S. Mahajan, J. J. Baumberg, O. A. Scherman, *J. Phys. Chem. Lett.* **2016**, *7*, 704.
- [19] J. P. Vivek, I. J. Burgess, *Langmuir* **2012**, *28*, 5040.
- [20] N. G. Bastús, J. Comenge, V. Puntès, *Langmuir* **2011**, *27*, 11098.
- [21] R. J. Hunter, *Zeta Potential in Colloid Science*, Elsevier, New York **1981**.
- [22] B. de Nijs, M. Kamp, I. Szabó, S. J. Barrow, F. Benz, G. Wu, C. Carnegie, R. Chikkaraddy, W. Wang, W. M. Deacon, E. Rosta, J. J. Baumberg, O. A. Scherman, *Faraday Discuss.* **2017**, *205*, 505.
- [23] G. L. Long, J. D. Winefordner, *Anal. Chem.* **1983**, *55*, 1432.
- [24] A. Martín, J. J. Wang, D. Iacopino, *RSC Adv.* **2014**, *4*, 20038.
- [25] N. V. Godoy, D. García-Lojo, F. A. Sigoli, J. Pérez-Juste, I. Pastoriza-Santos, I. O. Mazali, *Sens. Actuators, B* **2020**, *320*, 128412.
- [26] D. García-Lojo, S. Gómez-Graña, V. F. Martín, D. M. Solís, J. M. Taboada, J. Pérez-Juste, I. Pastoriza-Santos, *ACS Appl. Mater. Interfaces* **2020**, *12*, 46557.
- [27] C. Levene, E. Correa, E. W. Blanch, R. Goodacre, *Anal. Chem.* **2012**, *84*, 7899.
- [28] Y. Liu, J. Bao, L. Zhang, C. Chao, J. Guo, Y. Cheng, Y. Zhu, G. Xu, *Sens. Actuators, B* **2018**, *255*, 110.
- [29] D. Zhang, H. You, L. Zhang, J. Fang, *Anal. Chem.* **2020**, *92*, 15379.
- [30] P. Li, H. He, D. Lin, L. Yang, *Analyst* **2019**, *144*, 7406.
- [31] M. R. El-Zahry, *J. Anal. Methods Chem.* **2018**, *2018*, 9065249.
- [32] K. J. Si, P. Guo, Q. Shi, W. Cheng, *Anal. Chem.* **2015**, *87*, 5263.
- [33] L. Štolcová, V. Peksa, J. Proška, M. Procházka, *J. Raman Spectrosc.* **2018**, *49*, 499.
- [34] V. Burtsev, M. Erzina, O. Guselnikova, E. Miliutina, Y. Kalachyova, V. Svorcik, O. Lyutakov, *Analyst* **2021**, *146*, 3686.
- [35] M. L. de Souza, J. C. Otero, I. López-Tocón, *Nanomaterials* **2020**, *10*, 2339.

- [36] M. R. El-Zahry, I. H. Refaat, H. A. Mohamed, B. Lendl, *Anal. Bioanal. Chem.* **2016**, *408*, 4733.
- [37] Y.-L. Sung, F. Zhao, J. Li, W.-C. Shih, in *2016 IEEE SENSORS*, IEEE, Piscataway, NJ **2016**, pp. 1–3.
- [38] N. M. Rabovsky, I. K. Lednev, *Chem. Soc. Rev.* **2020**, *49*, 49.
- [39] K. He, X. Zhang, S. Ren, J. Sun, in *2016 IEEE Conf. Computer Vision and Pattern Recognition (CVPR)*, IEEE, Las Vegas, NV, USA **2016**.
- [40] X. Chen, L. Xie, Y. He, T. Guan, X. Zhou, B. Wang, G. Feng, H. Yu, Y. Ji, *Analyst* **2019**, *144*, 4312.
- [41] C.-S. Ho, N. Jean, C. A. Hogan, L. Blackmon, S. S. Jeffrey, M. Holodniy, N. Banaei, A. A. E. Saleh, S. Ermon, J. Dionne, *Nat. Commun.* **2019**, *10*, 4927.
- [42] S. A. Abdelaziz Ismael, A. Mohammed, H. Hefny, *Artif. Intell. Med.* **2020**, *102*, 101779.
- [43] X. Fan, W. Ming, H. Zeng, Z. Zhang, H. Lu, *Analyst* **2019**, *144*.
- [44] W. Jeon, C. B. Shin, *Chem. Eng. J.* **2009**, *152*, 575.
- [45] C. Y. Lee, W. T. Wang, C. C. Liu, L. M. Fu, *Chem. Eng. J.* **2016**, *288*, 146.
- [46] R. G. Woolford, *Can. J. Chem.* **1962**, *40*, 1846.
- [47] M. J. Abraham, T. Murtola, R. Schulz, S. Páll, J. C. Smith, B. Hess, E. Lindahl, *SoftwareX* **2015**, *1*, 19.
- [48] K. Vanommeslaeghe, E. Hatcher, C. Acharya, S. Kundu, S. Zhong, J. Shim, E. Darian, O. Guvench, P. Lopes, I. Vorobyov, A. D. Mackerell, *J. Comput. Chem.* **2009**, *31*, 371.
- [49] H. Heinz, R. A. Vaia, B. L. Farmer, R. R. Naik, *J. Phys. Chem. C* **2008**, *112*, 17281.
- [50] K. Vanommeslaeghe, A. D. MacKerell, *J. Chem. Inf. Model.* **2012**, *52*, 3144.
- [51] Z.-M. Zhang, S. Chen, Y.-Z. Liang, *Analyst* **2010**, *135*, 1138.
- [52] S. Fekri-Ershad, *Expert Syst. Appl.* **2020**, *158*, 113509.